IEEE Access
Multidisciplinary ⋮ Rapid Review ⋮ Open Access Journal

Received 11 December 2025, accepted 23 December 2025, date of publication 29 December 2025,
date of current version 2 January 2026.

Digital Object Identifier 10.1109/ACCESS.2025.3649293

RESEARCH ARTICLE

Interference Mitigation in One-Way Channel Reconstruction for Robust Phase-Based Ranging

GREGA MORANO, (Graduate Student Member, IEEE), TOMAŽ JAVORNIK, (Member, IEEE), ALEŠ SIMONČIČ, (Student Member, IEEE), ALEŠ ŠVIGELJ, (Senior Member, IEEE), AND ANDREJ HROVAT, (Member, IEEE)
Department of Communication Systems, Jožef Stefan Institute, 1000 Ljubljana, Slovenia
Jožef Stefan International Postgraduate School, 1000 Ljubljana, Slovenia

Corresponding author: Grega Morano (grega.morano@ijs.si)

This work was supported by Slovenian Research and Innovation Agency (ARIS) under Grant J2-4461 and Grant P2-0016.

ABSTRACT Under the Integrated Sensing and Communication (ISAC) paradigm, wireless networks are evolving into multifunctional platforms that seamlessly combine data transmission with high-precision ranging for applications such as indoor navigation, asset tracking, and context-aware Internet of Things (IoT). The Multi-Carrier Phase Difference (MCPD) method has emerged as an effective technique for enabling localization in narrowband communication systems by estimating the channel frequency response (CFR) used for distance estimation. Converting the two-way CFR (TWCFR) into a one-way CFR (OWCFR) provides a physically consistent representation of the propagation channel and thus improves the ranging performance. However, existing channel reconstruction (CR) methods rely on noise-sensitive phase unwrapping which degrades in the presence of noise and interference, common in dense IoT deployments and crowded frequency bands. To address these limitations, we propose a noise-resistant OWCFR reconstruction algorithm that utilizes a peak-driven adaptive windowing strategy to generate a reference TWCFR for reliable square-root branch selection and incorporates a delay alignment correction to restore the maximum unambiguous range. Simulation and experimental results using IEEE 802.15.4 time-slotted channel hopping (TSCH) compliant devices demonstrate that the proposed method achieves robust and accurate distance estimation in more than 99.8% of interference scenarios.

INDEX TERMS Bluetooth, channel frequency response (CFR), channel impulse response (CIR), IEEE 802.15.4, localization, multi-carrier phase difference (MCPD), one-way ranging, phase-based ranging (PBR), time slotted channel hopping (TSCH), two-way ranging.

I. INTRODUCTION

Wireless communication systems are rapidly evolving from single-purpose transmission systems to versatile platforms that seamlessly integrate sensing, localization, and information exchange [1]. Adopting the Integrated Sensing and Communication (ISAC) paradigm, wireless networks no longer treat localization as a supplementary feature but embed sensing capabilities alongside conventional data transmission [2]. This evolution is driven by a variety of applications that require indoor positioning and navigation, real-time asset tracking, and secure, location-based access control.

Empowering smart home and Internet of Things (IoT) ecosystems, ISAC combines seamless connectivity with precise localization, enabling context-aware automation and intelligent interaction with the environment, such as collaborative robots for household chores, presence-based ambient control or touchless home appliances [2], [3]. In industrial IoT, factories and warehouses can achieve greater efficiency and safety through systems that combine communication and precise tracking of assets and personnel [4], [5]. Urban infrastructures can benefit from integrated systems that provide both connectivity and situational awareness, improving services such as traffic management,

The associate editor coordinating the review of this manuscript and approving it for publication was Fang Yang.

crowd management, and public safety in smart cities [6], [7].

Distance estimation between devices is the first and essential step in most localization schemes and can be obtained by measuring physical signal properties such as received signal strength (RSS), time-of-arrival (ToA), or phase of the signal. Practical IoT deployments with low-cost narrowband radios cannot support the wide bandwidth or high sampling rates that conventional ToA techniques require [8], [9]. As a result, IoT systems are often limited to coarse positioning via RSS, which does not provide the accuracy required for indoor navigation, precision asset tracking, and collaborative robotics applications [10]. Phase-based ranging (PBR) overcomes this constraint by estimating distance through phase shifts introduced by the signal propagation path. With the multi-carrier phase difference (MCPD) technique [11], devices can estimate their mutual distance with a decimeter-level accuracy without the need for wide system bandwidth [12], [13]. The potential of PBR has been recognized by several research works that have investigated its incorporation into IoT communication technologies, including Bluetooth [11], [14], IEEE 802.15.4 [15], [16] and RFID [17]. These studies demonstrate that accurate ranging can be achieved with low-cost narrowband devices, enabling localization alongside existing communication. Recently, the Bluetooth Special Interest Group (SIG) included MCPD in the new channel sounding feature of the Bluetooth Core Specification version 6.0, marking the first standardization of PBR within a widely adopted IoT protocol [18], [19].

In a PBR process, the wireless channel is first sampled using the MCPD technique, where two devices estimate the channel frequency response (CFR) by sequentially hopping across multiple frequencies and capturing the phase of the received signal at each step. A key advantage of MCPD is its ability to resolve the initial phase offsets introduced by the phase-locked loops (PLLs) in each device, which would otherwise distort the measurements. Phase mismatches are eliminated by multiplying the measured one-way CFR (OWCFR) from both devices, producing a two-way CFR (TWCFR) that has traditionally served as the basis for range estimation. Due to the harmonic nature of the measured CFR, different spectral analysis techniques can be used to extract the distance.

Early phase-slope methods estimate the range from the slope of the CFR phase [11], [20], but can model only a single propagation path and therefore suffer from bias in multipath conditions. Fourier transform (FT)-based methods address this limitation by transforming the CFR into a channel impulse response (CIR), which reveals the underlying propagation delays of the line-of-sight (LoS) and multipath components (MPCs), enabling robust range estimation. Variants of FT-based methods have been proposed [21], [22], and comparative studies show that FT-based estimators outperform phase-slope methods [19], [23]. Although FT-based estimators are robust at low signal-to-noise ratio (SNR) conditions, their accuracy is limited by the Fourier resolution set by the available bandwidth (BW). In [24] the author proposed an iterative Bayesian refinement approach to improve the separability of closely spaced MPCs.

Subspace-based range estimation methods decompose the measured CFR into signal and noise subspaces and construct a pseudo-spectrum, where distinct peaks appear at the propagation delays corresponding to the true signal paths. As demonstrated in [12], the MUltiple SIgnal Classification (MUSIC) algorithm can achieve super-resolution when spatial smoothing is applied to the CFR to decorrelate closely spaced MPCs. Later work improved the accuracy and performance of the MUSIC framework by incorporating bandwidth extrapolation of the measured CFR, multi-antenna combining and reduced-complexity pseudo-spectrum computation [8]. In [25] the authors introduced a signal-subspace decomposition (SSD) approach with a long-short term memory (LSTM) model that provides improved distance estimation accuracy compared to MUSIC estimators. Data-driven range estimation approaches have also been explored. Support vector regression (SVR) models have been used to map CFR spectral features to distance estimates [26], and deep learning (DL) models have been trained on spatially smoothed CFR representations [9], both outperforming subspace-based range estimation in indoor environments.

In the conventional PBR pipeline, the estimated TWCFR is passed directly to the range estimation block, as shown in Fig. 1. However, the two-way response produced by MCPD represents a squared version of the physical channel, which contains apparent multipath components that distort the delay structure and reduce ranging accuracy [12], [27], [28]. The limitation can be addressed by introducing a channel reconstruction (CR) stage before range estimation. The goal of CR is to recover an OWCFR from the measured TWCFR and improve range estimation performance.

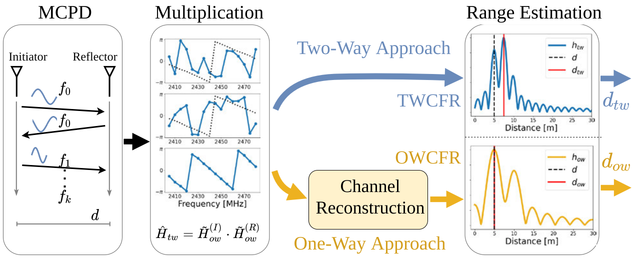

FIGURE 1. **Overview of the PBR process. The conventional two-way approach estimates the range directly from the TWCFR, while the one-way approach introduces a CR stage that recovers an OWCFR and improves the ranging performance.**

The CR process begins with a square root operation on the TWCFR, which introduces a sign ambiguity that must be resolved. In [29], authors propose to determine the correct sign by comparing the square root TWCFR with the measured OWCFR of one node. The approach relies on maintaining PLL locked when switching between carriers, and requires the time interval between initiator and reflector measurements to remain constant, as any significant timing mismatch can cause a root-flip error. These stringent PLL and timing requirements inherently limit the applicability of the solution to systems with dedicated hardware.

A more generalized approach was presented in [27], which determines the correct sign by applying phase unwrapping and threshold detection. The proposed approach also extends OWCFR reconstruction to non-contiguous frequency channels, making it applicable to wireless systems operating across multiple bands. However, the method is limited by the accuracy of phase unwrapping, which becomes challenging in the presence of noise in the measured phase. Measurement deviations can confuse the unwrapping algorithm, making the CR method unreliable.

In practical deployments, these deviations arise from hardware fluctuations, sampling techniques, or electromagnetic interference. The 2.4 GHz industrial, scientific, and medical (ISM) band, for example, accommodates numerous wireless technologies, resulting in overlapping transmissions, transient collisions, and variable noise levels. As the number of IoT devices increases [28], the likelihood of spurious emissions and unpredictable interference also increases. ISAC systems compound the problem by introducing dedicated sensing signals alongside traditional data signals, intensifying self-interference in the network, further degrading phase measurement quality, and exacerbating the limitations of OWCFR reconstruction based on phase unwrapping.

In this paper, we propose an enhanced CR algorithm that improves the performance of OWCFR restoration in the presence of noise caused by low SNR values, interference, or compressed sampling techniques. The main contributions of this paper are:

- We develop a branch-selective CR method that switches between square-root TWCFR phase branches using denoised wrap indices to reconstruct a OWCFRthat is consistent with the underlying propagation geometry, while remaining robust to interference and noise.
- We propose a dynamic, peak-driven strategy that identifies dominant CIR peaks and adaptively selects windows around them to generate a noise-reduced reference TWCFR for square-root branch selection.
- We introduce a delay alignment correction to restore the unambiguous range lost during OWCFR reconstruction.
- We validate our approach through simulations and real-world experiments on IEEE 802.15.4 platforms, demonstrating robust performance in multipath and high-interference environments.

The remainder of this paper is organized as follows. Section II presents the PBR and signal model, formalizing the MCPD distance estimation, range estimation, and CR process. This section also introduces the delay alignment correction to recover the full unambiguous range. Section III details our branch-selective OWCFR reconstruction method and the dynamic peak-driven windowing technique. Section IVcompares the computational complexity of the proposed method with baseline CR schemes. Section V outlines the simulation framework and evaluates performance under synthetic channel models. In addition, it describes the collection of real-world data and presents the corresponding experimental results. Section VII provides parameter sensitivity results and discusses the limitations and advantages of the proposed method. Finally, Section VII concludes the paper and discusses directions for future research. The key acronyms and variables used in this paper are summarized in Tables 1 and 2, respectively.

TABLE 1. List of key acronyms.

Acronym	Full Form
MCPD	Multi-Carrier Phase Difference
CFR	Channel Frequency Response
OWCFR	One-Way Channel Frequency Response
TWCFR	Two-Way Channel Frequency Response
CIR	Channel Impulse Response
OWCIR	One-Way Channel Impulse Response
TWCIR	Two-Way Channel Impulse Response
BW	Bandwidth
HPBW	Half-Power Beam Width
UR	Unambiguous Range
UT	Unambiguous Time
FFT	Fast Fourier Transform
iFFT	Inverse Fast Fourier Transform
PLL	Phase-Locked Loop
LoS	Line-of-Sight
MPC	Multipath Component
SNR	Signal-to-Noise Ratio
SIR	Signal-to-Interference Ratio
AWGN	Additive White Gaussian Noise
CR	Channel Reconstruction
CR-DT	Channel Reconstruction with Δt
CR-PU	Channel Reconstruction with Phase Unwrapping
CR-BS	Channel Reconstruction with Branch Selection

Notations: Throughout the paper, $H[\cdot]$ and $h[\cdot]$ denote the discrete CFR and its corresponding time domain CIR, respectively. Subscripts $(\cdot)_{ow}$ and $(\cdot)_{tw}$ indicate one-way and two-way quantities, subscript $(\cdot)_k$ indexes the carrier frequency, while $(\cdot)_l$ and $(\cdot)_m$ label propagation paths. Superscripts $(\cdot)^{(I)}$ and $(\cdot)^{(R)}$ refer to the initiator and reflector nodes, and superscripts such as $(\cdot)^{(DT)}$, $(\cdot)^{(PU)}$ and $(\cdot)^{(BS)}$ distinguish the different reconstruction methods. We use $\angle\cdot$ and $|\cdot|$ for phase and magnitude, $(\cdot)^*$ for complex conjugation, and $\underset{K}{\circledast}$ for circular convolution of length K. Ideal quantities appear without decoration, measured quantities are marked with a tilde $\widetilde{(\cdot)}$, estimated quantities use a hat $\widehat{(\cdot)}$, and filtered quantities use a bar $\overline{(\cdot)}$.

II. PHASE-BASED RANGING

PBR maps phase measurements to a distance estimate between two devices. The pipeline consists of three stages: MCPD acquisition, an optional CR stage, and range estimation. In the conventional two-way approach, the TWCFR from MCPD is passed directly to range estimation, as shown in Fig. 1. In the one-way approach, the additional CR stage

TABLE 2. List of key variables.

Variable	Notation	Description
Ideal OWCFR	H_{ow}	One-way CFR with assumed perfect phase coherency and no noise
Measured OWCFR at initiator	$\widetilde{H}_{ow}^{(I)}$	Phase incoherent one-way CFR measured at initiator node
Measured OWCFR at reflector	$\widetilde{H}_{ow}^{(R)}$	Phase incoherent one-way CFR measured at reflector node
Estimated TWCFR	$\widehat{H}_{tw}$	Two-way CFR obtained by multiplying estimated CFRs from nodes
Noise-reduced TWCFR	$\overline{\widehat{H}}_{tw}$	Windowed two-way CFR with suppressed noise
Square root of the TWCFR	$\widehat{H}_{sqrt}$	Complex square root of the estimated two-way CFR
Estimated OWCFR from CR-DT	$\widehat{H}_{ow}^{(DT)}$	Reconstructed one-way CFR obtained with channel reconstruction method presented in [29]
Estimated OWCFR from CR-PU	$\widehat{H}_{ow}^{(PU)}$	Reconstructed one-way CFR obtained with channel reconstruction method presented in [27]
Estimated OWCFR from CR-BS	$\widehat{H}_{ow}^{(BS)}$	Reconstructed one-way CFR obtained with channel reconstruction method proposed in this paper
UT delay of OWCIR	$T_{0,ow}$	Largest unambiguous time delay that can be estimated from one-way CIR
UT delay of TWCIR	$T_{0,tw}$	Largest unambiguous time delay that can be estimated from two-way CIR

processes the TWCFR to recover an effective OWCFR that more closely follows the true physical channel. The following subsections describe the three stages in more detail.

A. MCPD TECHNIQUE

The MCPD ranging procedure leverages phase measurements across multiple carrier frequencies to estimate the distance between two devices. By adopting an active reflector (AR) technique [20], one device acts as the initiator and the other as the reflector, exchanging continuous wave tones at K frequencies over the available bandwidth (BW), and sampling the in-phase and quadrature (I/Q) components of the received signals. Although early MCPD implementations relied solely on phase measurements, it is now recognized that incorporating amplitude information can further improve distance estimation [12]. The measured OWCFR at the reflector $\widetilde{H}_{ow}^{(R)}$ can be expressed as

$$\widetilde{H}_{ow}^{(R)}[k] = \sum_{l=1}^{L} a_l e^{-j\left(2\pi f_k(\tau_l - \Delta t) - (\phi_k^{(I)} - \phi_k^{(R)})\right)} + \eta_k^{(R)}, \qquad (1)$$

and in the measured OWCFR at the initiator $\widetilde{H}_{ow}^{(I)}$ can be expressed as

$$\widetilde{H}_{ow}^{(I)}[k] = \sum_{l=1}^{L} a_l e^{-j\left(2\pi f_k(\tau_l + \Delta t) - (\phi_k^{(R)} - \phi_k^{(I)})\right)} + \eta_k^{(I)}, \qquad (2)$$

where f_k is the kth carrier frequency at which the measurement was taken, L is the number of superimposed signal paths, a_l is the amplitude and τ_l is the propagation time of the lth path, Δt is the time difference between the initiator and the reflector, ϕ_k is the initial PLL phase offset of a device, and $\eta_k^{(I)}$ and $\eta_k^{(R)}$ are the assumed additive white Gaussian noise (AWGN) terms for the measurement at kth frequency. Following the MCPD technique, the measured CFR from the reflector is communicated back to the initiator where the two CFRs are multiplied to eliminate the time and phase offsets. The resulting estimated TWCFR $\widehat{H}_{tw}$ for the kth frequency is

$$\widehat{H}_{tw}[k] = \widetilde{H}_{ow}^{(I)}[k] \cdot \widetilde{H}_{ow}^{(R)}[k] = \sum_{m=1}^{M} a_m e^{-j2(2\pi f_k \tau_m)} + \widehat{\eta}_k, \quad (3)$$

where M is the number of newly created signal components, each with the corresponding amplitude a_m and propagation delay τ_m, and $\widehat{\eta}_k$ is the noise component at frequency k, arising from the squared and cross terms of the one-way noise.

B. RANGE ESTIMATION

The range estimation stage converts the measured CFR into an estimate of the propagation distance between the initiator and the reflector. Depending on the processing pipeline, the input to this stage is either the TWCFR produced by MCPD or an OWCFR estimate produced by the CR stage. Several range estimators have been proposed. Subspace-based and data-driven methods can provide enhanced resolution within the same BW, but they depend on design choices such as the assumed number of signal components and model training. In contrast, FT-based analysis applies a deterministic transform to the measured CFR and produces a distance estimate without tuning or training. Although not optimal in terms of absolute ranging accuracy, FT-based range estimation provides a reproducible and transparent baseline suitable for assessing the impact of the CR stage, which is the main focus of this paper.

The FT-based range estimator transforms the obtained CFR into a CIR, identifies the LoS component, and multiplies its propagation delay by the speed of light c_0 to estimate the distance. As the CFR is measured at discrete frequency points, the CIR is obtained using the inverse discrete Fourier transform (iDFT), which is typically implemented by the inverse fast Fourier transform (iFFT) algorithm. The iFFT maps the K collected frequency-domain samples, which are equally spaced with frequency step Δf over a total bandwidth $BW = K\Delta f$, into K time-domain taps ($n = 0, \ldots, K-1$) with:

$$h[n] = \text{iDFT}\{H[k]\} = \sum_{m=1}^{M} \alpha_m \, \delta\big[n - n_m\big] + v[n], \qquad (4)$$

where α_m denotes the complex amplitude of the mth path, and n_m is the discrete time index corresponding to the propagation delay τ_m, given by $n_m = \frac{\tau_m}{T_s}$. The time resolution T_s is determined by the measurement BW with $T_s = \frac{1}{BW}$. The term $v[n]$ represents noise in the time domain, obtained as the inverse transform of the frequency-domain noise. The resulting CIR $h[n]$ spans a time window $T_0 =$

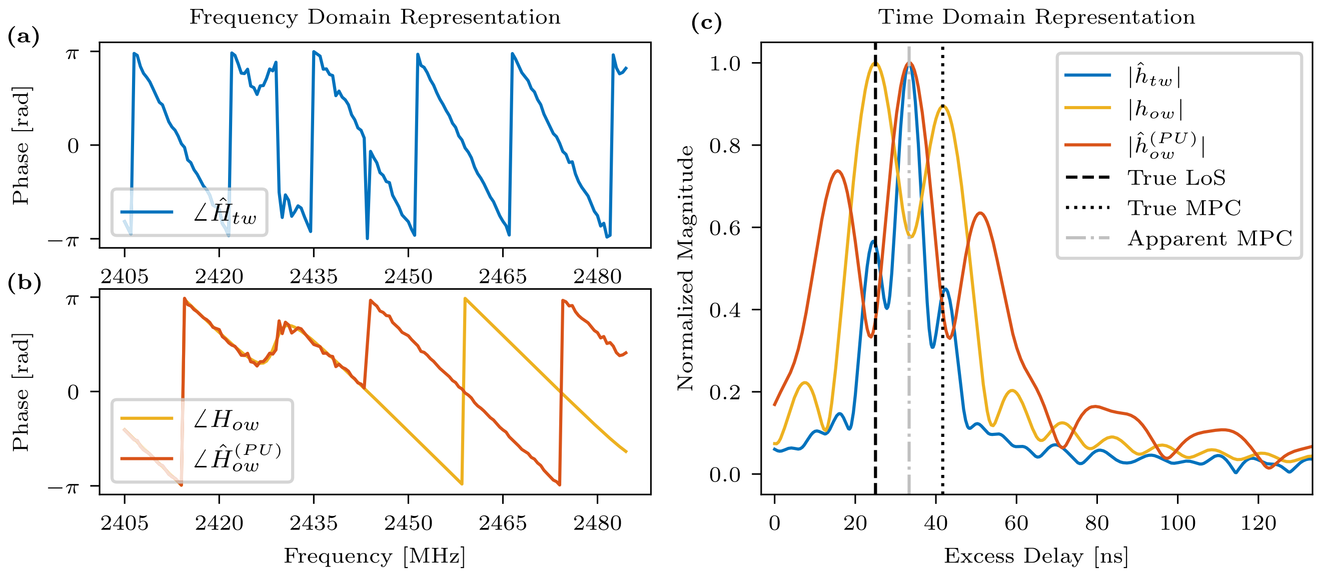

FIGURE 2. **An example of a noisy two-tap channel with interference in a single frequency bin at 2442 Mhz. (a) Phase plot of the estimated TWCFR ($\widehat{H}_{tw}$). (b) Phase of the ideal OWCFR (H_{ow}) and the reconstructed OWCFR ($\widehat{H}_{ow}^{(PU)}$) based on CR-PU method, that incorrectly unwraps at 2442 MHz. (c) Corresponding normalized impulse response magnitudes: TWCIR ($\widehat{h}_{tw}$) shows $M = 3$ paths with incorrect delays and magnitudes; the ideal OWCIR (h_{ow}) correctly identifies the LoS path (vertical dashed line) and MPC (vertical dotted line) whereas the one-way reconstruction based on CR-PU ($\widehat{h}_{ow}^{(PU)}$) erroneously restores the CIR.**

$K\,T_s$, which defines the maximum unambiguous time (UT) delay and consequently the unambiguous range (UR) over which the MPCs can be distinguished. The CIR appears as a sparse sequence of complex-valued Dirac delta pulses, each corresponding to a propagation path m. Examining the CIR magnitude $|h[n]|$, the height of each peak reflects the amplitude of that path and its position indicates the path delay. The first (and often largest) peak is usually the direct LoS component of interest, while the subsequent smaller peaks arise from reflections and scattering, representing the MPCs.

C. CHANNEL RECONSTRUCTION

The CR stage modifies the output of MCPD before range estimation to align the effective channel representation with the physical one-way propagation. Multiplying the two measured OWCFRs in the MCPD stage mitigates initial phase mismatches and time synchronization effects. In the time domain, multiplication is equivalent to a circular convolution of the two one-way CIRs (OWCIRs):

$$\widehat{h}_{tw}[n] = \widetilde{h}_{ow}^{(I)}[n] \underset{K}{\circledast} \widetilde{h}_{ow}^{(R)}[n]. \tag{5}$$

As a result of the convolution, the two-way CIR (TWCIR) contains an increased number of delay paths M compared to the number of delay paths L in the OWCIR:

$$M = L + \binom{L}{2} = \frac{L(L+1)}{2}, \tag{6}$$

as shown in Fig. 2 (c). The extra taps appear as apparent MPCs, which weaken the true first tap representing the LoS path, making its detection more difficult and reducing ranging accuracy in multipath-rich environments [27]. The introduction of apparent MPCs makes the CIR unusable for sensing applications that require accurate multipath characterization. Furthermore, the multiplication process combines noise from both CFR measurements, increasing the overall noise level in the TWCFR and spreading the channel power over more taps, which reduces their magnitude and can render some undetectable [27].

The CR stage addresses some drawbacks by inserting an intermediate processing block between MCPD and range estimation. The purpose of CR is to reverse the convolution effects and recover a representation that closely resembles the original OWCIR, thereby removing apparent MPCs, restoring the strength of the LoS component, and improving distance estimation. Reconstruction begins by taking the complex square root of the estimated TWCFR and selecting the principal branch, producing $\widehat{H}_{sqrt}$ as follows:

$$\widehat{H}_{sqrt}[k] = b_k\sqrt{\widehat{H}_{tw}[k]}, \quad \text{where } b_k \in \pm 1. \tag{7}$$

The square root operation introduces a sign ambiguity b_k that must be resolved across the carrier frequency index k. When the sequence of signs is recovered correctly, $\widehat{H}_{sqrt}$ coincides with the OWCFR, effectively reconstructing the OWCFR from the TWCFR. Any error in the sequence produces a mismatched OWCFR that generates a CIR unrelated to the true OWCIR and renders the measurement completely unusable.

In [29] the authors propose finding the correct signs b_k by comparing the measured OWCFR of one device with the square root of the TWCFR, evaluating $\Theta[k] = \angle(\widetilde{H}_{ow}^{(I)}[k] \cdot \widehat{H}_{sqrt}^{*}[k])$. Using (2), (3), and (7), we obtain

$$\Theta[k] = 2\pi f_k \Delta t - \Delta\phi_k, \qquad \Delta\phi_k = \phi_k^{(R)} - \phi_k^{(I)}. \tag{8}$$

Assuming that the PLL remains locked when switching from frequency index k to $k+1$ so that $\Delta\phi_{k+1} = \Delta\phi_k$, the time difference Δt can be estimated as

$$\widehat{\Delta t} = \frac{\Theta[k+1] - \Theta[k]}{2\pi\Delta f}. \tag{9}$$

Since MCPD guarantees that Δt is constant across all carrier frequencies, $\widehat{\Delta t}$ makes a distinct jump at indices k where $\widehat{H}_{sqrt}[k]$ exhibits an incorrect sign. The jump pattern helps resolve the ambiguity in (7) and enables reconstruction of the OWCFR, denoted $\widehat{H}_{ow}^{(DT)}$. Hereafter, we refer to the described reconstruction approach as CR-DT.

However, the CR-DT method can be used only when the PLL remains locked during frequency transitions in the MCPD technique. A more general approach that relaxes the PLL design requirements was presented in [27], which determines the correct sign using phase unwrapping. Specifically, the proposed method analyzes the phase slope of the square root of the TWCFR, $\widehat{H}_{sqrt}$, and identifies the frequency indices where the phase difference between consecutive samples exceeds $\frac{\pi}{2}$. By unwrapping the phase at the detected indices, the method reconstructs the OWCFR, denoted as $\widehat{H}_{ow}^{(PU)}$. Hereafter, we refer to the described CR approach based on phase unwrapping as CR-PU.

D. UNAMBIGUOUS RANGE

Although the effects of CFR multiplication on distance estimation results are well understood [27], its reduction of the maximum UT delay, and therefore the UR of the CIR remain largely unexamined, leaving an important parameter unaddressed by earlier work. For an ideal OWCFR sampled with a frequency step Δf, the FFT-based analysis produces an OWCIR with a period of $T_{0,ow} = KT_s = \frac{1}{\Delta f}$. When two one-way measurements are multiplied to obtain a TWCFR, the corresponding delay-domain operation is a circular convolution of the two impulse responses. The (5) can be rewritten as:

$$\widehat{h}_{tw}[n] = \sum_{p=0}^{K-1} \widetilde{h}_{ow}^{(I)}[p]\, \widetilde{h}_{ow}^{(R)}\big[(n-p) \bmod K\big]. \tag{10}$$

Although convolution increases the time support of the impulse response to twice its original width $2K$, the circular nature (modulo K) folds the indices $n \geq K$ back into the interval $[0, K-1]$. Consequently, the section of $\widehat{h}_{tw}[n]$ that remains alias-free is limited to the first $\frac{K}{2}$ samples, and therefore the maximum UT delay is reduced from $T_{0,ow} = \frac{1}{\Delta f}$ for a one-way measurement to:

$$T_{0,tw} = \frac{K}{2}\, T_s = \frac{1}{2\Delta f}, \tag{11}$$

for a two-way measurement. Any signal propagation component with an excess delay $\tau_m > T_{0,tw}$ is cyclically aliased into the interval $[0, T_{0,tw})$, making the overall interpretation of the impulse response unreliable. Therefore, we recommend using a sufficiently small frequency step during measurements so that practical propagation delays remain below the $T_{0,tw}$ threshold. For example, with $\Delta f = 1$ MHz, common in Bluetooth PBR, the two-way unambiguous delay becomes $T_{0.tw} = 500$ ns, which corresponds to an unambiguous distance of approximately 150 m.

Taking the square root of the TWCFR and resolving the sign ambiguity in the CR stage does not remove the aliasing caused by the circular convolution of the two one-way impulse responses. In fact, under certain propagation conditions, the reconstructed OWCIR may even be shifted from the first to the second half of the delay window, as illustrated in Fig. 3. To clarify the origin of the CIR shift, we examine the incremental phase of the two-way response from (3), defined as:

$$\Delta\Phi_{tw} = \angle\widehat{H}_{tw}[k+1] - \angle\widehat{H}_{tw}[k] \approx -4\pi\Delta f\tau. \tag{12}$$

As the time delay (τ) between the transceivers increases, $\Delta\Phi_{tw}$ decreases linearly from 0 to $-\pi$. At certain delay value, denoted τ_{wrap}, the incremental phase reaches $-\pi$ and wraps to $+\pi$. Beyond τ_{wrap} the incremental phase continues to decrease until it reaches 0 again.

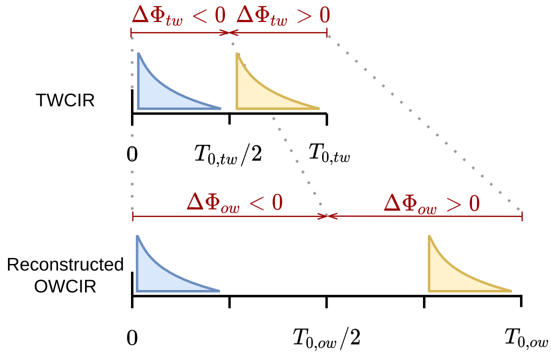

FIGURE 3. OWCIR reconstruction follows the phase slope of the TWCFR $\Delta\Phi_{tw}$. When the average $\Delta\Phi_{tw}$ is negative, the recovered OWCIR maps correctly; when it is positive, the reconstructed OWCIR is shifted by half the delay window ($T_{ow}/2$).

By analyzing the τ_{wrap} for the two-way and one-way channel representations, we can observe that the TWCFR completes a π cycle after only half the delay interval required an ideal OWCFR:

$$-4\pi\Delta f\tau_{wrap} = -\pi \;\Rightarrow\; \tau_{wrap} = \frac{1}{4\Delta f} = \frac{T_{0,tw}}{2} = \frac{T_{0,ow}}{4}. \tag{13}$$

Since the CR procedure follows the TWCFR phase and interprets $\Delta\Phi_{tw}$ as a one-way phase difference, two distinct reconstructions can occur:

- For channels whose energy is mainly concentrated at delays smaller than τ_{wrap}, the average $\Delta\Phi_{tw}$ is negative, so the recovered OWCIR maps correctly to the interval $[0,\ T_{0,ow}/2]$, where negative phase slopes are expected (Fig. 3 blue shape).
- For channels whose dominant energy lies above τ_{wrap}, the average $\Delta\Phi_{tw}$ appears positive, shifting the reconstructed OWCIR to $[T_{0,ow}/2,\ T_{0,ow}]$ (Fig. 3 yellow

shape). In this case, the estimated propagation delay is systematically greater by $T_{0,ow}/2$.

If left unaddressed, this shift reduces the UT of the reconstructed OWCFR to $T_{0,ow}/4$, further constraining the maximum resolvable range. To compensate for CIR misplacement, we apply a simple alignment correction. For each estimated delay $\hat{\tau}$ obtained from the reconstructed OWCIR we define

$$\hat{\tau}_{corr} = \begin{cases} \hat{\tau}, & \hat{\tau} \leq T_{0,ow}/2, \\ \hat{\tau} - T_{0,ow}/2, & \hat{\tau} > T_{0,ow}/2, \end{cases} \tag{14}$$

which maps the corrected delay estimate $\hat{\tau}_{corr}$ back to the physically valid interval $[0, T_{0,ow}/2)$ and restores the full one-way UR.

III. ROBUST OWCFR RECONSTRUCTION

A key weakness in resolving the sign ambiguity in (7) using either CR-DT or CR-PU methods is their sensitivity to measurement deviations. The existing CR methods perform reliably only under high SNR conditions and when the phase slope of the TWCFR is sufficiently small. However, under realistic conditions, several factors introduce or amplify noise in the measured TWCFR, significantly degrading the effectiveness of the CR. First, random fluctuations in hardware and the environment cause unpredictable phase changes, corrupting the measured phase response. Second, in MCPD systems where measurements are taken sequentially at multiple frequencies, external interference at one or more frequencies can produce erroneous phase estimates [28], causing strong deviations in the samples. Third, compressed sampling approaches that extrapolate the TWCFR from fewer samples can introduce additional deviations in the phase [16].

Such deviations in estimated TWCFR can cause incorrect CR for any distance within the UR, as illustrated in Fig. 2, where a single corrupted measurement leads to failure. Larger distances between devices further increase the difficulty in selecting the correct sign b_k, because the phase slope of the TWCFR increases as the range approaches half the UT. For CR-PU, the problem is particularly severe, as the method relies on comparing the phase of two consecutive measurements whose values become nearly π apart near $T_0/2$, leaving no tolerance for small measurement deviations. Any failure in the unwrapping step results in a reconstructed OWCFR that no longer reflects the true channel and becomes unusable for ranging.

To address the identified limitations, we propose a noise resistant CR that resolves the square root ambiguity in (7) using a denoised reference extracted from the estimated TWCFR ($\widehat{H}_{tw}$). The method operates in three steps: 1) peak search, 2) windowing, and 3) square root branch selection, as summarized in Fig. 4. The first two steps generate a noise reduced TWCFR reference $\overline{\widehat{H}}_{tw}$, which is then used in the final step to determine the correct square root branch and obtain the reconstructed OWCFR $\widehat{H}_{ow}^{(BS)}$. Unlike CR-DT, the proposed method does not require the PLL to remain locked during frequency transitions in MCPD. In addition, the reconstruction is performed on each individual TWCFR measurement without temporal averaging or repeated acquisitions, enabling a single shot operation. Hereafter, we refer to the proposed branch selective reconstruction method as CR-BS. Algorithm 1 summarizes the complete procedure.

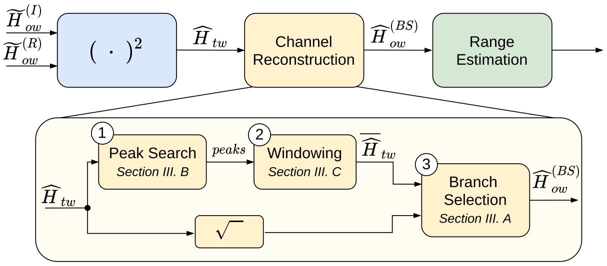

FIGURE 4. The workflow diagram of the proposed CR-BS method.

A. SQUARE-ROOT BRANCH SELECTION

The core of the proposed CR-BS method is the selection of the correct square root branch in (7) across the carrier index k. Rather than relying on raw phase differences of the estimated TWCFR, which are highly sensitive to noise and interference bursts, the proposed approach anchors all sign transitions to indices where a phase wrap is detected in a noise-reduced TWCFR reference. The reference is constructed through the peak detection and windowing steps introduced later in the section.

The reconstruction begins with the square root of the TWCFR, yielding two possible phase curves by considering the principal branch of the square root $+\sqrt{\widehat{H}_{tw}}$ and its negative branch $-\sqrt{\widehat{H}_{tw}}$, as shown in Fig. 5 (b). The positive branch is selected initially, and its progression is followed until a full phase wrap is detected in the denoised TWCFR reference $\overline{\widehat{H}}_{tw}$. A wrap is declared at carrier index k whenever the difference $|\angle\overline{\widehat{H}}_{tw}[k] - \angle\overline{\widehat{H}}_{tw}[k-1]| \geq \pi$. At each detected wrap index, the opposite branch is selected, and that trajectory is followed until the next wrap. Repeating this process across the carrier index aligns the evolution of the square root with the physical progression of the true one-way channel response and reconstructs the OWCFR $\widehat{H}_{ow}^{(BS)}$. By guiding branch switching with stable wrap points extracted from the denoised reference, the CR-BS produces a consistent OWCFR and avoids erroneous sign flips that affect CR-DT and CR-PU under practical conditions, as illustrated in Fig. 5 (c).

It is important to note that the denoised reference is not used directly to reconstruct the OWCFR. Applying CR-PU or related methods directly to the filtered TWCFR ($\overline{\widehat{H}}_{tw}$) would distort the results, as windowing may suppress parts of the delay profile that belong to the true channel. Instead, the filtered TWCFR is used only to identify reliable wrap indices, while the actual reconstruction is performed on the original estimated TWCFR ($\widehat{H}_{tw}$). Separation ensures that the reconstructed OWCFR preserves the true channel structure when the full square root sequence is stitched together.

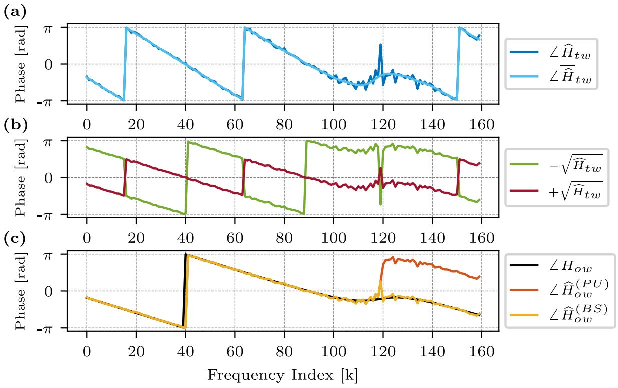

FIGURE 5. (a) Phase of the measured TWCFR $\widehat{H}_{tw}$ and its noise-reduced reference $\overline{\widehat{H}}_{tw}$ used to identify genuine 2π wraps (frequency indexes: 15, 63 and 150). (b) The square root of $\widehat{H}_{tw}$ yields two interleaved phase curves for the positive and negative root branches. (c) CR-BS method begins on the positive root branch and switches the branch at each detected wrap index, ensuring correct one-way phase traversal. The $\widehat{H}_{ow}^{(PU)}$ makes an error at index 119, whereas $\widehat{H}_{ow}^{(BS)}$ correctly follows the ideal OWCFR H_{ow}.

An effective approach to obtain a noise-reduced TWCFR is to transform the estimated channel into the time domain, where the inherent sparsity of the CIR enables easier identification and isolation of signal components. The measured CIR displays distinct peaks corresponding to different signal propagation paths, with noise superimposing additional spurious peaks. To retain only the primary CIR and reduce noise, the true path-induced components are detected and isolated, while the rest of the delay profile is suppressed. In this paper, we propose a windowing technique based on the dynamic identification of CIR peaks and the application of corresponding bandpass windows aligned to the delay of each detected path. Transforming the filtered CIR back into the frequency domain yields a de-noised TWCFR, which serves as a reliable reference for the subsequent branch selection step.

B. PEAK DETECTION

Identifying signal components by detecting peaks in the CIR is challenging in noisy environments, as spurious noise can produce false peaks. To obtain a reference $\overline{\widehat{H}}_{tw}$, we propose defining a fixed amplitude threshold in the CIR and selecting every peak that exceeds this threshold as a signal component. Although a threshold-based approach may occasionally omit very weak multipath arrivals or include a noise artifact, it provides a simple and repeatable procedure for isolating the dominant contributors to the CFR.

Algorithm 1 Channel Reconstruction With Branch Selection

```
Input: $\widehat{H}_{tw}, P, F$
Output: $\widehat{H}_{ow}^{(BS)}$
Initialization:
$K \leftarrow$ length($\widehat{H}_{tw}$)
peaks $\leftarrow$ [ ]
$W \leftarrow$ ones($K$)
Procedure:
    // Step 1: Peak search with threshold
win $\leftarrow$ Hann($K$)
$\widehat{h}_{tw} \leftarrow$ IFFT($\widehat{H}_{tw} \cdot$ win)
PDP $\leftarrow |\widehat{h}_{tw}|^2$
CDF $\leftarrow$ sort(PDP)
dCDF $\leftarrow$ differentiate(CDF)
TH$_P \leftarrow$ max(dCDF) $\cdot P$
relmax $\leftarrow$ relmax(PDP) // indices of local maxima
for each $p$inrelmax do
    if $PDP[p] \geq TH_P$ then
        append $p$topeaks
    end if
end for
    // Step 2: Window segments and product of complements
for each $\tau_i$inpeaks do
    $\Delta_i \leftarrow$ HPBW($\tau_i$) $\cdot F$ // Half-power width of peak $\tau_i$
    if $\Delta_i > K$ then
        $\Delta_i \leftarrow K$
    end if
    segment $\leftarrow$ Hann($\Delta_i$)
    $w_i \leftarrow$ zeros($K$)
    for $l = 0$to$\Delta_i - 1$ do
        $l_{circ} \leftarrow (l - \lfloor \Delta_i/2 \rfloor + \tau_i) \bmod K$
        $w_i[l_{circ}] \leftarrow$ segment[$l$]
    end for
    $W \leftarrow W \cdot (1 - w_i)$
end for
$W \leftarrow 1 - W$
$\overline{\widehat{h}}_{tw} \leftarrow W \cdot \widehat{h}_{tw}$
$\overline{\widehat{H}}_{tw} \leftarrow$ FFT($\overline{\widehat{h}}_{tw}$)
    // Step 3: Branch selection based on $\overline{\widehat{H}}_{tw}$
$\phi \leftarrow \angle \overline{\widehat{H}}_{tw}$
$\widehat{H}_{sqrt} \leftarrow \sqrt{\widehat{H}_{tw}}$
$b \leftarrow 1$
for $k = 1$ to $K - 1$ do
    if $|\phi[k] - \phi[k-1]| > \pi$ then
        $b \leftarrow -b$
    end if
    $\widehat{H}_{ow}^{(BS)}[k] \leftarrow b \cdot \widehat{H}_{sqrt}[k]$
end for
return $\widehat{H}_{ow}^{(BS)}$
```

The threshold is determined by squaring the absolute CIR to obtain a power delay profile (PDP) and sorting the samples by amplitude to generate an empirical cumulative distribution function (CDF) curve, as shown in Fig. 6. In a typical sparse channel, the curve begins with a long, gently rising tail that represents the noise floor values, followed by a convex increase toward the end of the curve, which corresponds to the peak values from the PDP. In low-noise channels, the knee index of the CDF, i.e. the point of maximum curvature, effectively separates the noise-related values from the steep ascent caused by the peak values. This knee can be identified

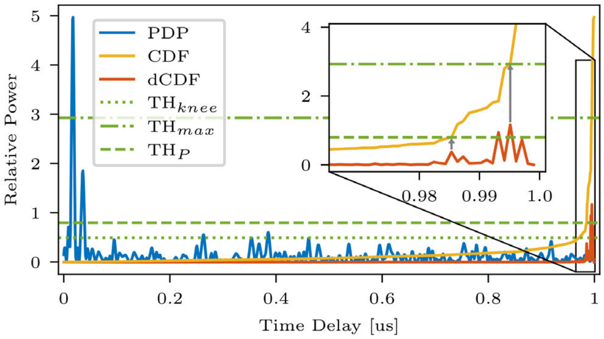

FIGURE 6. **The operation of the peak search algorithm in noisy two-tap channel. The PDP is plotted in blue, its CDF in yellow and the derivative of the CDF in red. The threshold obtained with knee method TH_{knee} erroneously classifies noise-related peaks as weak multipath components. The threshold based on the maximum of the CDF derivative TH_{max} recognizes the dominant peak, while the threshold based on a fraction P of the maximum derivative TH_P correctly identifies both signal components and avoids the noise.**

using the curvature-based method described in [30] and the threshold (TH_{knee}) is defined as the PDP value at the knee location index. However, as noise variance increases, noise-related peak values raise the tail of the CDF curve, causing the knee detector to frequently misidentify noise peaks as weak multipath components, thereby reducing the robustness of the peak detection process.

To better align threshold selection with the shape of the PDP, we analyze the rate of change in the empirical CDF. Its derivative curve (dCDF) displays distinct spikes, each corresponding to a jump in the CDF caused by high peak values in the PDP. Although the maximum derivative indicates the largest jump in the CDF and thus the strongest peak in the PDP, we instead define the threshold using the index of the first occurrence where the derivative exceeds a fraction P of that maximum. The value of the PDP at this index is taken as the peak search threshold TH_P. The approach ensures that peaks of meaningful magnitude are preserved while ignoring noisy variations, and provides a flexible mechanism to adapt the threshold to different propagation environments. For example, a lower P (e.g., 0.2) will admit more moderate reflections in multipath-rich scenarios, while a higher P (e.g., 0.5) will focus exclusively on the very strong paths common in sparse settings.

C. DYNAMIC WINDOW DESIGN

The purpose of windowing is to isolate the signal's components of interest while attenuating the noise-dominated regions. We observed the following design criteria for effective window design:

- **Sufficient bandpass width**: The window must be wide enough to capture all relevant information from the signal components.
- **Smooth transition**: An abrupt drop from the bandpass to the bandstop (a "sharp window") can introduce undesirable phase distortions. Therefore, a gradual roll-off in the window is essential to minimize unwanted phase shifts.

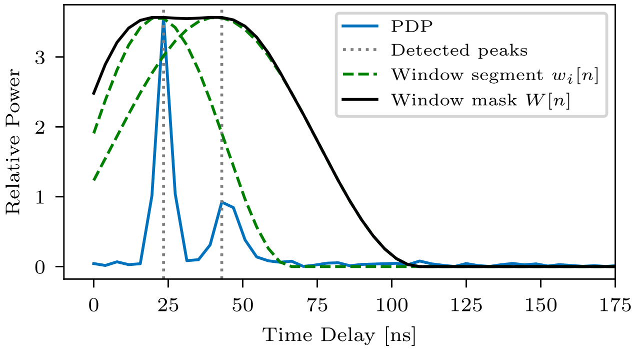

FIGURE 7. **The PDP (blue curve) with individual Hann windows w_i (dashed green curve) centered at each detected peak τ_i (dotted gray line). The windows w_i are merged into a single composite window mask W, wrapping around the borders of the PDP. Note that the rightmost window w_i is wider, reflecting the broader HPBW.**

- **Periodicity**: As the FFT representation of the CIR is inherently periodic, the window must maintain this periodicity. If the detected peak lies near the edge of the CIR, the window should roll over to the other side, ensuring continuity for the iFFT.

Building on the dynamic peak-driven windowing framework, we formalized the construction of individual narrow windows centered on each detected CIR peak and the procedure for combining them into a unified composite filter mask, as shown in Fig. 7. To isolate the spectral contributions of distinct propagation components, a finite-length Hann window $w_i[n]$ is centered at each detected delay τ_i:

$$w_i[n] = \begin{cases} 0.5\left[1-\cos\left(2\pi\frac{n-\left(\tau_i-\frac{\Delta_i}{2}\right)}{\Delta_i-1}\right)\right], & |n-\tau_i| \le \frac{\Delta_i}{2}, \\ 0, & \text{otherwise.} \end{cases} \tag{15}$$

The window span Δ_i is calculated from the half-power beam width (HPBW) of the i-th peak (the difference between the two delay indices where the PDP envelope falls to the half of the peak value) and is scaled by a factor F to capture side lobes and deep fade regions. Isolated propagation paths produce sharp peaks, while densely clustered multipath arrivals produce broader features. Using HPBW to determine the width of each window enables the filter span to adapt intrinsically to the local multipath density.

If any window extends beyond the edges $[0, K]$ of the PDP interval, its samples wrap around modulo K to maintain the inherent periodicity of FFT. The individual window segments $w_i[n]$ are then merged into a single smooth composite mask $W[n]$ through the algebraic sum merge:

$$W[n] = 1 - \prod_{i=1}^{I}(1 - w_i[n]), \tag{16}$$

where I is the total number of detected peaks. This "fuzzy union" operation retains the individual Hann window shapes in regions without overlap and smoothly saturates towards unity where overlaps occur, resulting in a composite mask that preserves all signal components while effectively suppressing noise.

IV. COMPUTATIONAL COMPLEXITY

PBR is typically implemented on resource constrained IoT devices, where computational load is an important design factor. In this section, we analyze the computational complexity of the proposed CR-BS algorithm and compare it with the CR-DT and CR-PU baseline methods to assess their feasibility on embedded platforms.

The proposed CR-BS consists of three stages, as shown in the diagram in Fig. 4. In the first stage, the TWCFR is windowed, transformed to the time domain, and used to identify signals of interest, where I denotes the number of detected peaks, and $I < K$. In the second stage, the samples around each peak are windowed with the global weighting function W, producing the filtered TWCFR. In the third stage, the denoised TWCFR is used for branch selection, reconstructing the OWCFR. The three steps contribute to the overall time complexity function:

$$T(K, I) = T_{peak}(K) + T_{win}(K, I) + T_{bs}(K). \tag{17}$$

The initial CFR windowing requires $2K$ operations, while the subsequent K point IFFT has a cost of $\frac{3K}{2} \log K$. The computation of the PDP and its CDF involves sorting the K values, contributing another $K \log K$ operations. The CDF differentiation, search for local maxima and amplitude thresholding are performed through linear scans, each requiring K operations. Selecting the valid peaks then requires I comparisons. Hence, the total complexity of the peak search stage is

$$T_{peak}(K) = O(K \log K). \tag{18}$$

For each detected peak τ_i the algorithm generates a window segment of length Δ_i, performs circular indexing to place it on a grid of length K, and updates the global window W via elementwise multiplication. The computational cost for a single peak is therefore $2K + 2\Delta_i$. The cost of constructing a global window over I peaks is $O\big(IK + \sum_{i=1}^{I} \Delta_i\big)$. Since $\Delta_i \leq K$ for all peaks, the total cost is dominated by $O(IK)$. Afterwards, the denoising is performed with multiplication of TWCIR and W which requires K operations, followed by FFT of length K to reconstruct the filtered TWCFR, contributing $\frac{3K}{2} \log K$ operations. The cost function of the windowing stage becomes

$$T_{win}(K, I) = O(IK + K \log K). \tag{19}$$

In branch selection, the computation of the filtered TWCFR phase, the square root operation on the TWCFR, and the phase jump-based branch selection loop each require K operations. Therefore,

$$T_{bs}(K) = O(K). \tag{20}$$

Combining the stages yields

$$T(K, I) = O(IK + K \log K + K). \tag{21}$$

TABLE 3. Asymptotic time complexity of CR algorithms for TWCFR of *K* carrier frequencies.

Algorithm	Computational Complexity
CR-DT	$O(K)$
CR-PU	$O(K)$
CR-BS	$O(K \log K)$

In the worst case scenario, where half of the points in the PDP are selected as detected peaks and $I = \frac{K}{2}$ the complexity becomes quadratic, $O(K^2)$. However, in typical sparse multipath channels, the number of significant detected peaks I is small and does not increase with K. In this regime, the dominant cost arises from the two FFT operations and the sorting algorithm, giving the final time complexity

$$T(K) = O(K \log K). \tag{22}$$

For comparison, the baseline methods CR-PU and CR-DT have linear complexity in the number of carrier frequencies K. The CR-PU method first applies the square root to the TWCFR and then unwraps the phase across the K carrier frequencies. Both operations require K steps, so the overall complexity is $O(K)$. The CR-DT method applies the square root to the TWCFR, forms a product sequence by combining the square root of the TWCFR with the measured CFR of one device, computes the time difference, detects phase jumps, and constructs and applies the correction mask. Each of the five steps requires K operations, so the complexity of CR-DT also grows linearly with K. The asymptotic time complexity of the three algorithms is summarized in Table 3.

The proposed CR-BS algorithm introduces an additional logarithmic factor in time complexity compared to CR-DT and CR-PU. This additional cost is mainly due to the FFT operations and the sorting step in the peak search stage. Nonetheless, in the complete PBR pipeline, the dominant computational cost often arises in the subsequent range estimation step. In case of FT-based analysis, the input CFR is typically interpolated by zero padding to improve the accuracy of delay estimation, and processed by an iFFT with a size significantly larger than the number of measured carriers K. The computational complexity of such range estimation exceeds the cost of CR-BS, so the additional CR stage has a low impact on overall runtime. The per snapshot cost of CR-BS is therefore within capabilities of resource-constrained IoT and modern embedded platforms that already implement FT-based range estimators. In exchange for the increased computational load, CR-BS provides a significant improvement in robustness of OWCFR reconstruction in the presence of noise and interference, as demonstrated in the following Section V.

V. EVALUATION OF THE PROPOSED METHOD

The evaluation of the proposed algorithm is divided into two parts: simulation-based results and results from real-world deployments. Simulations enable analysis of the

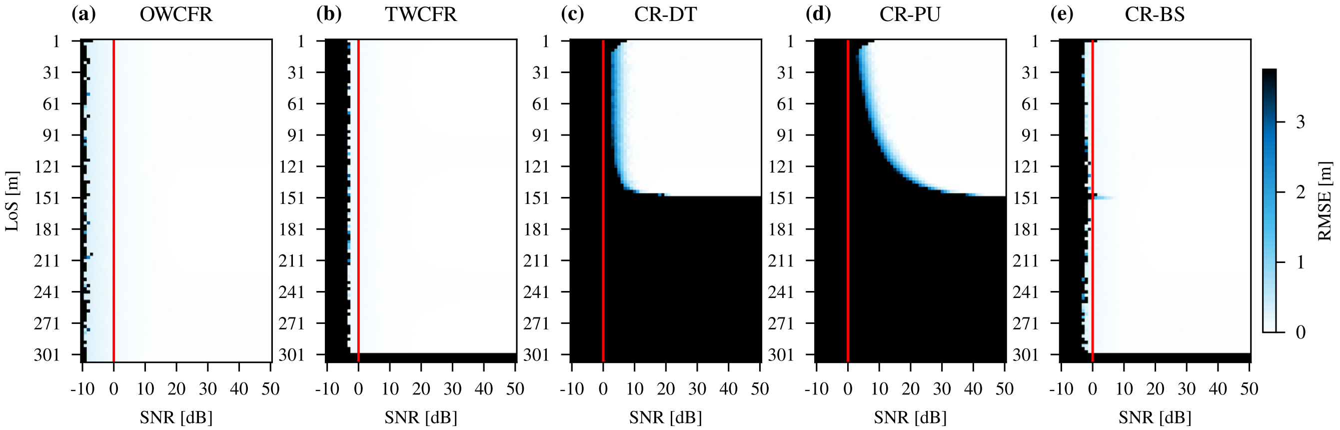

FIGURE 8. RMSE of distance estimation for a single-tap simulation. Plots (a) to (e) present the RMSE obtained when the range estimator uses different CFR inputs, namely: (a) ideal OWCFR (H_{ow}), (b) estimated TWCFR ($\widehat{H}_{tw}$), (c) estimated OWCFR from the CR-DT method ($\widehat{H}_{ow}^{(DT)}$), (d) estimated OWCFR from the CR-PU method ($\widehat{H}_{ow}^{(PU)}$), and (e) estimated OWCFR from the proposed CR-BS method ($\widehat{H}_{ow}^{(BS)}$). For ease of comparison, the 0 dB SNR level is indicated with red vertical line.

algorithm under edge-case conditions, while measurements provide valuable insights into its practical operability. For all experiments, the range estimation stage was carried out with a fixed FT-based procedure. The estimated CFR was zero-padded to 8192 bins, and an iFFT was applied to generate the corresponding CIR. The propagation delay was then extracted as the delay of the maximum peak in the CIR and multiplied by the speed of light to obtain the estimated distance. The unified processing chain allowed for direct comparison of the CR-PU, CR-DT and CR-BS methods without bias from additional range estimator design choices. For the proposed CR-BS algorithm, the following values were used: the peak search parameter P was set to 0.2 and the window factor F to 10, unless stated otherwise.

A. SIMULATION RESULTS

The simulations were performed using a custom-designed simulation framework that emulates the MCPD algorithm. The simulator takes propagation delays and their corresponding amplitudes as input and then synthesizes the CFR measurements of the initiator and reflector over 160 frequency carriers uniformly spaced from 2405 MHz to 2484.5 MHz. AWGN is added according to a specified SNR. The noise power is derived from the average received signal power, computed as the sum of the mean powers received across all propagation paths. For the analysis, ideal synchronization is assumed, meaning that there is no carrier frequency offset or clock drift between devices. Although CFO or clock drift can introduce a linear phase slope across frequencies that affects the absolute range estimate [13], they do not introduce abrupt phase discontinuities that cause failures in CR methods, which are the focus of the analysis.

Firstly, a single propagation path was considered and the distance between the devices was swept from 1 m to 304 m in steps of 3 m. Signal attenuation along this LoS path was modeled using the free-space path loss propagation model. As only a very strong LoS component is expected, the parameter P of the CR-BS algorithm is set to 0.5. Fig. 8 shows the root mean square error (RMSE) of 500 independent distance estimations for SNRs ranging from -10 dB to 50 dB, where the RMSE is capped at 3.75 m as errors above this threshold render the measurement unusable. It can be observed that the distance estimation results depend strongly on the CFR input provided to the range estimation stage.

When the ideal OWCFR is used as input (Figs. 8 (a)), the estimator operates at a lower SNR and maintains higher accuracy. When the estimated TWCFR is used (Figs. 8 (b)), the multiplication step introduces combined noise that increases the lower SNR limit of operation and degrades the accuracy of distance estimates. Although not fully depicted (the distance sweep was limited to 305 m for visual clarity), the ideal OWCFR supports distance estimation up to 600 m, while TWCFR measurements reach a maximum UR of only 300 m. The reduced limit is a side effect of the circular convolution that halves the UT of the two-way measurements. The results of the CR-DT method presented in Fig. 8 (c) show a limited operating region. Reliable distance estimation appears only at sufficiently high SNR (above 5 dB) and the maximum operational range remains below 150 m ($c_0 \frac{T_{0,ow}}{4}$). Outside the reliable region, the CR-DT method does not preserve the true one-way channel representation, leading to large errors in distance estimation. The CR-PU results in Fig. 8(d) show an even more restricted region of correct operation as the distance between devices increases. The increased RMSE can be attributed to the phase unwrapping step, which compares the phase of two consecutive measurements whose values become nearly π apart around the 150 m, leaving no tolerance for small measurement deviations. Fig. 8 (d) presents the results of the proposed CR-BS. The method successfully resolves the range ambiguity for delays above $\frac{T_{0,ow}}{4}$ and reduces the lower limit of operation to SNR below 0 dB. A small degradation appears near 150 m, which is the same effect observed for the CR-DT and CR-PU methods, but the impact on CR-BS is considerably smaller. Notably, although

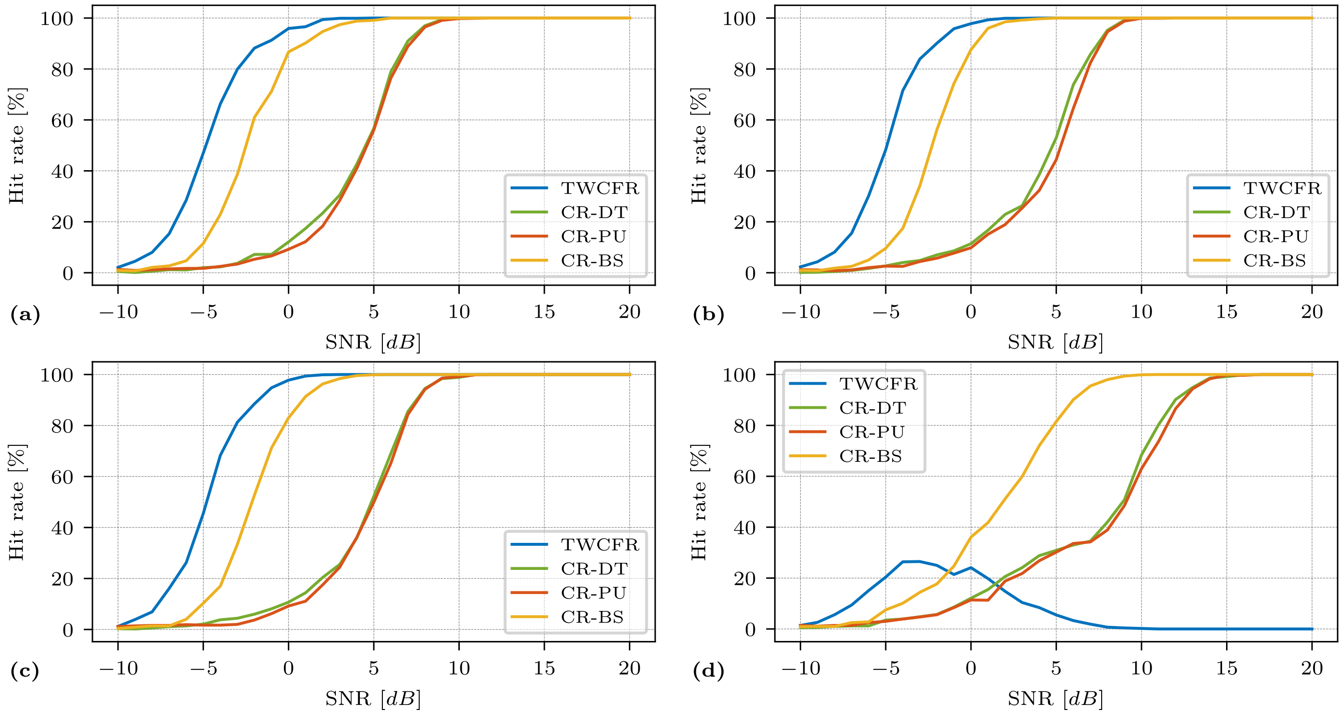

FIGURE 9. The percentage of distance estimates within ±12.5 cm of the true distance (hit rate) with standardized channel models: (a) TGn model B, (b) TGn model C, (c) TGn model D, and (d) TGn model B variant with the increased power of each path in the second cluster by 1.5 dB.

the proposed CR-BS reconstructs a one-way representation of the channel, the UT does not return to the ideal one-way limit and remains the same as that of the two-way channel.

To assess the robustness of the algorithm in more realistic propagation scenarios, we conducted additional simulations using standardized IEEE 802.11 TGn channel models [31]. We considered three LoS channel models: a) Model B (15 ns delay spread, two clusters), for small indoor environments such as offices, b) Model C (30 ns delay spread, two clusters), suited to larger indoor or mixed indoor/outdoor settings such as open-plan offices and hallways, and c) Model D (50 ns delay spread, three clusters), representing spacious environments such as large halls or classrooms, where richer multipath is expected. In addition to the standardized models, we analyzed a modified "high-reflection" variant of Model B, in which the power of every tap in the second cluster was increased by 1.5 dB. The proposed adjustment emulates environments with strong nearby reflectors (e.g., metallic furniture, computer monitors, or industrial equipment) and provides insight into the performance of the algorithm in wireless channels where two propagation paths produce an apparent multipath artifact caused by the multiplication of measured CFRs. AWGN was applied to each channel model over an SNR range of –10 dB to 20 dB in 1 dB increments. At each SNR step, 1000 independent distance estimates were generated from the corresponding CFRs, and the percentage of estimates within 0.25 m of the true distance (hit rate) was calculated. The results are presented in Fig. 9 where subplots (a), (b), and (c) show Models B, C, and D, respectively, while subplot (d) corresponds to the high-reflection variant of Model B.

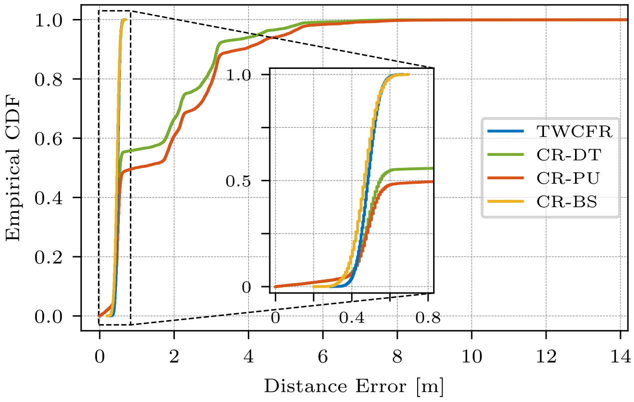

FIGURE 10. CDF of the absolute distance estimation error for the TGn channel model C operating at SNR of 5 dB. The inset provides a magnified view for clarity.

When the range estimation stage operates directly on the TWCFR input, the first three scenarios show nearly perfect hit rates for SNR values above 2 dB. However, these high hit rates conceal the fact that the resulting TWCIR contains apparent multipath components, rendering the impulse response unusable for sensing tasks that require an exact channel representation. The limitation becomes evident in the modified Model B scenario (Fig. 9 (d)), where an apparent peak introduced by the two-way operation dominates the true LoS component and causes the range estimator to select an incorrect delay. Consequently, the hit rate of the TWCFR input drops to zero, revealing a fundamental weakness in relying on two-way measurements in the range estimation stage. In contrast, the CR-DT and CR-PU provide a reconstructed OWCFR to the estimator and succeed in recovering the correct impulse response, but only when the SNR exceeds 15 dB. Below this level, their hit rates fall rapidly. The proposed CR-BS reduces the SNR requirement to below 10 dB and maintains high hit rates even in the presence of considerable noise.

The empirical cumulative distribution of absolute distance errors at an SNR of 5 dB for Model C, based on 10000 trials, is shown in Fig. 10. The zero-padding length for distance estimation was increased from 8192 to 65536 bins so that the CDF appears as a smooth curve rather than a stepped one. When the range estimation stage receives the OWCFR from CR-PU as input, phase unwrapping failures cause approximately half of the estimates to deviate by up to 8 m or more, rendering these measurements unusable. The CR-DT produces a similar distribution, with slightly better performance than CR-PU. The proposed CR-BS reconstruction removes the extreme errors and achieves a tighter error distribution, outperforming the TWCFR in the low SNR regime.

B. MEASUREMENTS WITH INTERFERENCE

The performance of the proposed algorithm was evaluated using real-world channel measurements taken in a conference room (4 m by 6 m) where magnetic boards mounted on the walls provided strong reflective surfaces for multipath components, as shown in Fig. 11. Two proprietary VESNA devices [32], equipped with an AT86RF215 radio supporting IQ sampling, probed the channel under a modified IEEE 802.15.4 Time Slotted Channel Hopping (TSCH) protocol [16] that enables seamless PBR alongside standard communication. Each device captured 160 IQ samples in the frequency range from 2400.5 MHz to 2480.0 MHz.

The transceivers were placed in three LoS configurations, Setup 1, Setup 2 and Setup 3 with separations of 2 m, 3 m and 4 m, respectively. The ground truth distances for all three setups were confirmed using a laser ranger. We obtained 2140 measurements in Setup 1, 2200 measurements in Setup 2 and 2015 measurements in Setup 3. Each distance estimate includes a fixed hardware offset caused by additional propagation paths through the antennas, cables, and circuit board traces. In our deployment, this offset was measured at 1.8 m. The resilience of the algorithm to in-band interference was assessed by injecting additive noise into IEEE 802.15.4 channel 19 (center frequency 2445 MHz and span of 5 MHz) in all three setups, so that the signal-to-interference ratio (SIR) was –3 dB.

Only three CFRs were evaluated in the measurement study: TWCFR and the OWCFRs obtained from the CR-PU and CR-BS methods. The CR-DT method was excluded because the radios used in the experiment do not enable PLL lock. Nonetheless, simulation analysis has already demonstrated that CR-PU performs comparably with CR-DT, so the exclusion of CR-DT does not affect the interpretation of the measurement results.

FIGURE 11. Measurements in a conference room with two magnetic whiteboards.

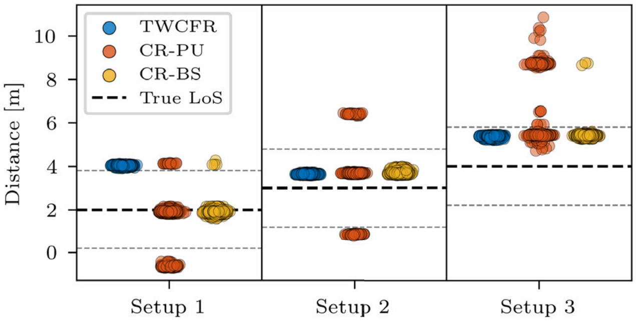

FIGURE 12. Estimated peak locations from real-world measurements with interference on channel 19. Each dot on the plot represents the location of a maximum peak for the estimated CIR.

The distance estimates obtained from different CFR across the setups are shown in Fig. 12. Each dot marks the position of the strongest CIR peak selected as the LoS component. In Setup 1, the TWCFR estimates cluster tightly around 4 m instead of the true 2 m because the multiplication artifact peak in TWCIR outweighs the actual LoS arrival peak and directs the estimator to an incorrect delay. The CR-PU method produces a more dispersed cloud of points that largely lie on the correct distance but occasionally fall below or above it, reflecting phase unwrapping failures caused by in-band interference on channel 19. Note that some of the plotted estimates fall below zero, which results from the hardware offset calibration. In contrast, the OWCFR of the proposed CR-BS method adheres to the 2 m reference line in 99.8 percent of all trials, confirming its ability to reconstruct the channel accurately even in the presence of interference.

An example of impulse responses from measurements in Setup 1 is shown in Fig. 13. The plot illustrates the combination of one-way peaks at 3.7 m and 8.4 m (at 1.9 m and 6.6 m after hardware offset calibration) to create the apparent two-way peak at 5.8 m (at 4 m after calibration). Additionally, the plot demonstrates an occasional distortion of distance estimation due to CR-PU creating a CIR that does not resemble the true channel. These real-world measurement

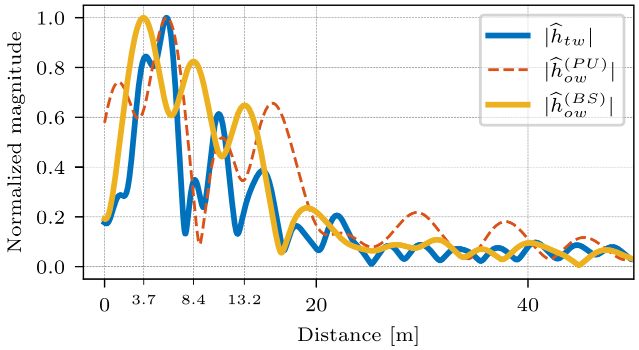

FIGURE 13. Example of CIR estimates from measurements in Setup 1. Since the x-axis is not calibrated for hardware distance offset, the LoS peak is located at 3.7 m instead of 2 m.

results also reveal the fundamental limitation of FT-based range estimation imposed by the 80 MHz measurement bandwidth. Closely spaced MPCs that fall within the $\frac{c_0}{BW}$ resolution merge into a single peak or shift each other through spectral leakage. This systematic error prevents any CR method from achieving perfect accuracy in Setups 2 and 3, where multiple reflections lie near the direct path.

Key error statistics across all three setups are summarized in Table 4. The mean absolute error (MAE) measures the average magnitude of the estimation errors, while the standard deviation (STD) quantifies the spread of those errors around the mean. The hit rate (HR) is the percentage of distance estimates that are within the ± 1.875 m of the true separation. This threshold was chosen to match the resolution of the FT-based range estimator, given by c_0/BW. In Setup 1 the CR-BS delivers highly accurate results, whereas the CR-PU shows high variability, with HR of only 84.5 percent and STD of 0.93 m. In Setup 2 both TWCFR and OWCFR from CR-BS achieve flawless HR with MAE values of 0.65 and 0.69 respectively, reflecting the systematic range estimation error due to bandwidth limitation. The CR-PU remains more erratic with HR of 84.6% and STD of 1.07 m. In Setup 3 the CR-BS again maintains its accuracy with 99.8% HR, while the CR-PU degrades to 78.6%. Overall, CR-BS consistently outperforms baseline methods by combining correct peak recovery with low variance, even under strong interference and across varying propagation channels.

C. MEASUREMENTS WITH COMPRESSED SAMPLING

We further validated the algorithm using a publicly available data set [16] that uses compressed sampling measurements in three real-world deployments: an indoor office, an indoor hallway, and an outdoor park. The measurements were obtained using a modified MCPD scheme, in which the Golomb ruler technique was used to reduce the number of carrier frequencies sampled, thereby decreasing interference with other devices and lowering the energy usage of the devices. After extraction of the samples, the CFR consists of 160 samples with a frequency step of $\Delta f = 0.5$ MHz. Fig. 14 shows the distance estimation results for the three scenarios with the true distance on the x-axis and the distance estimation on the y-axis. Each point in the plot corresponds to the median of the estimated distances, and the spline area around indicates the standard deviation of the estimations.

TABLE 4. Mean absolute error (MAE), standard deviation (STD), root mean square error (RMSE) and hit rate (HR) counting estimates within ± 1.875 m of the true distance.

		MAE [m]	STD [m]	RMSE [m]	HR [%]
Setup 1	TWCFR	2.054	0.025	2.054	0.0
	CR-PU	0.476	0.931	1.02	84.5
	CR-BS	0.104	0.111	0.143	99.8
Setup 2	TWCFR	0.649	0.017	0.649	100.0
	CR-PU	0.957	1.073	1.16	84.6
	CR-BS	0.695	0.065	0.698	100.0
Setup 3	TWCFR	1.394	0.033	1.394	100.0
	CR-PU	2.136	1.362	2.533	78.6
	CR-BS	1.426	0.132	1.432	99.8

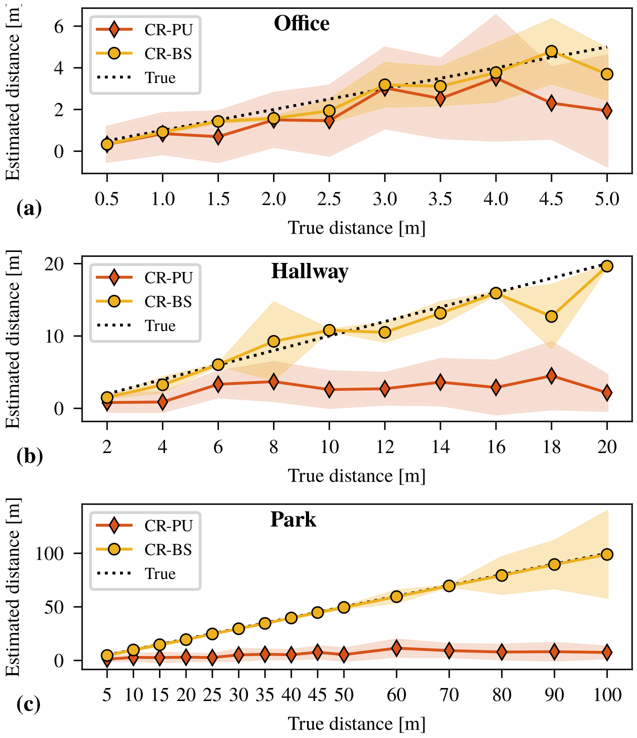

FIGURE 14. Real-world measurement results for: (a) indoor office, (b) indoor hallway and (c) outdoor park. Diamonds and dots denote the median distance estimates when the input for range estimation is obtained from the CR-DT and CR-BS, respectively. The shaded area represents the standard deviation of the measurements.

The compressed sampling technique introduces spikes in the phase response of the TWCFR, as presented in Fig. 15, which completely confuse the CR-PU reconstruction algorithm. As observed in Fig. 14, the algorithm functions only when the distance between devices is short, and otherwise fails to determine the correct distance. In contrast, the proposed CR-BS successfully reconstructs the OWCFR and with it the distance estimation in all three scenarios,

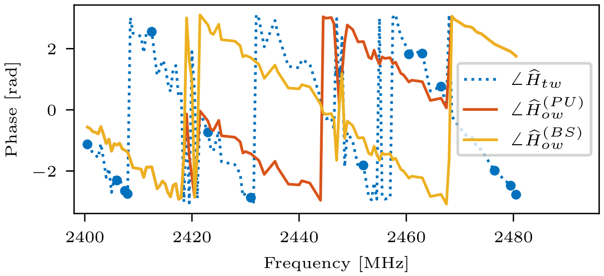

FIGURE 15. **Phase of the CFR estimates made using the Golomb ruler technique. The TWCFR is reconstructed by extrapolating 15 measured samples (marked with blue dots) to 160 points, introducing pronounced phase spikes (around 2420 and 2468 MHz) that confuse the phase unwrapping algorithm and render the OWCFR from CR-PU unreliable.**

with a noticeably lower standard deviation compared to the CR-PU.

VI. DISCUSSION

To assess the robustness of the proposed peak-driven windowing method, we conducted a detailed parameter sensitivity analysis focusing on the two key design parameters, the peak-selection threshold P and the window-scaling factor F. The evaluation was performed on a modified TGn model B channel. For SNR levels between −4 dB and 14 dB, we generated 1000 independent noisy realizations of the TWCFR. For each realization and every combination of P and F, we obtained the OWCFR from the CR-BS reconstruction, estimated the distance using the FT-based estimator, and recorded the hit rate as the percentage of cases in which the dominant CIR peak was within ±12.5 cm of the true delay.

The results, corresponding to P values of 0.01, 0.05, 0.1 and 0.5, are shown in the four subplots of Fig. 16 and reveal a clear interaction between the two parameters. When P is set very low, the peak detector accepts even weak noise-induced fluctuations, especially under low SNR conditions. When many peaks are falsely identified as valid signal components, numerous windows are created, collectively passing a significant amount of noise and reducing the hit rate. Increasing the threshold avoids spurious peak detections and improves performance, as only CIR peaks that correspond to actual propagation paths are admitted. For higher thresholds, such as $P = 0.1$ and $P = 0.5$, the algorithm identifies only the strongest components, so the window must be wider to capture the surrounding energy of the multipath features. Consequently, the best results for $P = 0.1$ and $P = 0.5$ are obtained when the window factor is approximately $F = 8$. Once P becomes sufficiently large to reliably exclude noise peaks, further increases of P do not significantly affect the behavior, and the performance curves become visually indistinguishable. Across all threshold levels, a consistent pattern emerges: wider windows allow more noise to pass through, and once F becomes excessively large the filter spans nearly the entire CIR, so performance gradually declines.

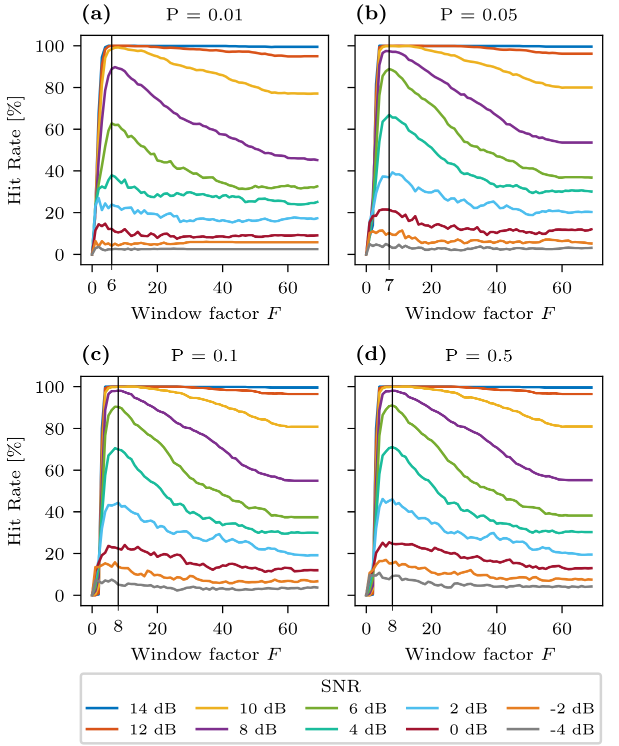

FIGURE 16. **Parameter sensitivity of the proposed method for the standardized BN channel model. Each subplot shows the hit rate of CR-BS performance as a function of the window factor *F* for a peak-selection threshold *P*: (a) 0.01, (b) 0.05, (c) 0.1 and (d) 0.5. Plot curves represent different SNR levels ranging from -4 dB to 14 dB. Results are obtained from 1000 simulations per SNR value.**

The main limitation of the proposed approach is the reliance on accurate peak detection and appropriate windowing. In scenarios with very weak or strongly overlapping MPCs, the thresholding strategy may fail to identify all physically significant peaks, leading to incomplete reconstruction. Similarly, an inappropriate choice of F can either truncate useful signal energy or admit excessive noise, making CR-BS performance sensitive to parameter tuning in channels that deviate from the assumed sparse multipath structure. Nonetheless, the overall study confirms that the proposed CR-BS is highly adaptable and that appropriate adjustment of P and F enables reliable reconstruction even under low SNR conditions.

The simulation and experimental results show that with 80 MHz measurement bandwidth, closely spaced MPCs partially overlap and become distorted through spectral leakage, producing a systematic range error that no CR method can resolve. CR-BS can restore the correct one-way structure at the available delay resolution, but it cannot separate MPCs that fall within the same delay bin or undo the bias caused by clusters that already appear as a single tap in the measured CIR. As a result, CR-BS improves the quality of the input to the range estimator, but the final distance estimate is still constrained by the sounding bandwidth and by the simple maximum peak rule in the FT-based estimator.

Another limitation of the proposed CR-BS method concerns computational complexity and, consequently, energy consumption on constrained IoT devices. As presented in Section IV, the proposed method imposes additional computational load compared to baseline CR methods. In channels with many significant MPCs, the constant factors in (21) increase, so the energy cost per ranging instance can rise even further. As a trade off, the higher complexity provides improved reconstruction accuracy and ranging performance compared to baseline CR methods, particularly in the presence of strong phase distortions and noise.

At the same time, CR-BS operates on a single snapshot of the TWCFR and does not rely on temporal averaging or tracking. Therefore, the method remains applicable in the presence of non-stationary interference and device mobility, provided that the MCPD frequency sweep is completed within the channel coherence time. Moreover, the algorithm works with the estimated TWCFR and is therefore independent of the underlying physical layer or protocol. Although the experiments are performed with a MCPD implementation in IEEE 802.15.4 TSCH hardware, the method is directly compatible with Bluetooth due to the shared multi-carrier channel sounding procedure, making the approach applicable to other practical PBR solutions.

VII. CONCLUSION

In this work, we propose CR-BS, a branch selective OWCFR reconstruction method that operates on noisy TWCFR measurements and recovers a one-way channel representation consistent with the underlying propagation channel. We also address the implicit misalignment of OWCIR caused by the reconstruction procedure and present a simple delay alignment correction to recover the full unambiguous range. In contrast to the baseline reconstruction schemes CR-PU and CR-DT, the proposed method enables reliable operation at lower SNR and under strong interference. Simulation results for single-tap and standardized multipath channel models demonstrate that our method lowers the operational SNR threshold to below 0 dB for single-path scenarios and below 10 dB in rich multipath, while maintaining the original maximum UR. Real-world measurements using IEEE 802.15.4 TSCH platforms, even under strong in-band interference and compressed sampling, confirm hit rates above 99% and robust one-way channel recovery, demonstrating that CR-BS provides a practical and reliable CR solution for low-cost PBR systems. In future work, we plan to integrate super-resolution range estimation algorithms to mitigate the systematic delay error introduced by bandwidth limitations and to analyze their operation in combination with our proposed OWCFR reconstruction method.

REFERENCES

[1] F. Liu, Y. Cui, C. Masouros, J. Xu, T. X. Han, Y. C. Eldar, and S. Buzzi, “Integrated sensing and communications: Toward dual-functional wireless networks for 6G and beyond,” *IEEE J. Sel. Areas Commun.*, vol. 40, no. 6, pp. 1728–1767, Jun. 2022.

[2] Y. Cui, F. Liu, X. Jing, and J. Mu, “Integrating sensing and communications for ubiquitous IoT: Applications, trends, and challenges,” *IEEE Netw.*, vol. 35, no. 5, pp. 158–167, Sep. 2021.

[3] F. Khelifi, A. Bradai, A. Benslimane, P. Rawat, and M. Atri, “A survey of localization systems in Internet of Things,” *Mobile Netw. Appl.*, vol. 24, no. 3, pp. 761–785, Jun. 2019.

[4] T. Savic, X. Vilajosana, and T. Watteyne, “Constrained localization: A survey,” *IEEE Access*, vol. 10, pp. 49297–49321, 2022.

[5] F. Zafari, A. Gkelias, and K. K. Leung, “A survey of indoor localization systems and technologies,” *IEEE Commun. Surv. Tut.*, vol. 21, no. 3, pp. 2568–2599, 3rd Quart., 2019.

[6] J. A. Zhang, M. L. Rahman, K. Wu, X. Huang, Y. J. Guo, S. Chen, and J. Yuan, “Enabling joint communication and radar sensing in mobile networks—A survey,” *IEEE Commun. Surv. Tut.*, vol. 24, no. 1, pp. 306–345, 1st Quart., 2022.

[7] F. Liu, C. Masouros, A. P. Petropulu, H. Griffiths, and L. Hanzo, “Joint radar and communication design: Applications, state-of-the-art, and the road ahead,” *IEEE Trans. Commun.*, vol. 68, no. 6, pp. 3834–3862, Jun. 2020.

[8] S. N. Shoudha, J. P. Van Marter, S. Helwa, A. G. Dabak, M. Torlak, and N. Al-Dhahir, “Reduced-complexity decimeter-level Bluetooth ranging in multipath environments,” *IEEE Access*, vol. 10, pp. 38335–38350, 2022.

[9] Z. Bin Tariq, J. P. Van Marter, A. G. Dabak, N. Al-Dhahir, and M. Torlak, “Reduced complexity deep learning approach for Bluetooth ranging in multipath environments,” *IEEE Sensors J.*, vol. 24, no. 19, pp. 31431–31441, Oct. 2024.

[10] A. Moradbeikie, A. Keshavarz, H. Rostami, S. Paiva, and S. I. Lopes, “A cost-effective LoRaWAN-based IoT localization method using fixed reference nodes and dual-slope path-loss modeling,” *Internet Things*, vol. 24, Dec. 2023, Art. no. 100990.

[11] P. Zand, J. Romme, J. Govers, F. Pasveer, and G. Dolmans, “A high-accuracy phase-based ranging solution with Bluetooth low energy (BLE),” in *Proc. IEEE Wireless Commun. Netw. Conf. (WCNC)*, Apr. 2019, pp. 1–8.

[12] P. Boer, J. Romme, J. Govers, and G. Dolmans, “Performance of high-accuracy phase-based ranging in multipath environments,” in *Proc. IEEE 91st Veh. Technol. Conf. (VTC-Spring)*, May 2020, pp. 1–5.

[13] A. Simončič, G. Morano, A. Hrovat, and T. Javornik, “Optimizing frequency switching pattern to reduce asynchronization effect in MCPD ranging systems,” *IEEE Access*, vol. 13, pp. 169791–169811, 2025.

[14] P. Zand, A. Duzen, J. Romme, J. Govers, C. Bachmann, and K. Philips, “A high-accuracy concurrent phase-based ranging for large-scale dense BLE network,” in *Proc. IEEE 30th Annu. Int. Symp. Pers., Indoor Mobile Radio Commun. (PIMRC)*, Sep. 2019, pp. 1–7.

[15] Y. Schröder and L. Wolf, “InPhase: Phase-based ranging and localization,” *ACM Trans. Sensor Netw.*, vol. 18, no. 2, pp. 1–39, Jan. 2022.

[16] G. Morano, K. Guan, A. Hrovat, and T. Javornik, “Phase-based distance estimation integrated with IEEE 802.15.4 TSCH communication,” *IEEE Internet Things J.*, vol. 11, no. 7, pp. 11460–11470, Apr. 2024.

[17] L. Xie, D. Jiang, X. Fu, and Q. Jiang, “Centimeter-level localization algorithm with RFID passive tags,” in *Wireless and Satellite Systems*, M. Jia, Q. Guo, and W. Meng, Eds., Cham, Switzerland: Springer, 2019, pp. 160–170.

[18] (Aug. 2024). *Bluetooth Core Specification*. [Online]. Available: https://www.bluetooth.com/specifications/specs/core-specification-6-0/

[19] M. Nikodem, G. Trajnowicz, G. S. de Blasio, and F. A. Quesada-Arencibia, “Experimental evaluation of multicarrier phase difference localization in Bluetooth low energy,” *IEEE Sensors J.*, vol. 25, no. 1, pp. 1548–1560, Jan. 2025.

[20] M. Pelka, C. Bollmeyer, and H. Hellbruck, “Accurate radio distance estimation by phase measurements with multiple frequencies,” in *Proc. Int. Conf. Indoor Positioning Indoor Navigat. (IPIN)*, Oct. 2014, pp. 142–151.

[21] G. von Zengen, Y. Schroder, S. Rottmann, F. Busching, and L. C. Wolf, “No-cost distance estimation using standard WSN radios,” in *Proc. IEEE 35th Annu. IEEE Int. Conf. Comput. Commun.*, Apr. 2016, pp. 1–9.

[22] Y. Schröder, D. Reimers, and L. Wolf, “Accurate and precise distance estimation from phase-based ranging data,” in *Proc. Int. Conf. Indoor Positioning Indoor Navigat. (IPIN)*, Sep. 2018, pp. 1–8.

[23] M. Gunia, A. Zinke, N. Joram, and F. Ellinger, “Setting up a phase-based positioning system using off-the-shelf components,” in *Proc. 14th Workshop Positioning, Navigat. Commun. (WPNC)*, Oct. 2017, pp. 1–6.

[24] J. Mazur, “High-resolution phase-based ranging using inverse Fourier transform in an iterative Bayesian approach,” *Sensors*, vol. 24, no. 20, p. 6758, Oct. 2024.

[25] Z. B. Tariq, J. P. Van Marter, A. G. Dabak, N. Al-Dhahir, and M. Torlak, "A data-driven signal subspace approach for indoor Bluetooth ranging," *IEEE J. Indoor Seamless Positioning Navigat.*, vol. 2, pp. 292–303, 2024.

[26] J. P. Van Marter, A. G. Dabak, N. Al-Dhahir, and M. Torlak, "Support vector regression for Bluetooth ranging in multipath environments," *IEEE Internet Things J.*, vol. 10, no. 13, pp. 11533–11546, Jul. 2023.

[27] S. Helwa, J. P. Van Marter, S. N. Shoudha, M. Ben-Shachar, Y. Alpert, A. G. Dabak, M. Torlak, and N. Al-Dhahir, "Bridging the performance gap between two-way and one-way CSI-based 5 GHz WiFi ranging," *IEEE Access*, vol. 11, pp. 70023–70039, 2023.

[28] A. Sheikh, J. Romme, J. Govers, A. Farsaei, and C. Bachmann, "Phase-based ranging in narrowband systems with missing/interfered tones," *IEEE Internet Things J.*, vol. 10, no. 17, pp. 15171–15185, Sep. 2023.

[29] J. Romme, "Method for distance determination," U.S. Patent 10 928 495 B2, Feb. 23, 2021.

[30] V. Satopaa, J. Albrecht, D. Irwin, and B. Raghavan, "Finding a, 'Kneedle' in a Haystack: Detecting Knee Points in System Behavior," in *Proc. 31st Int. Conf. Distrib. Comput. Syst. Workshops*, Jun. 2011, pp. 166–171.

[31] V. Erceg, *IEEE P802.11 Wireles LANs, TGn Channel Models*, Standard 802.11-03/940r4, May 2004.

[32] G. Morano, A. Simončič, T. Kocevska, T. Javornik, and A. Hrovat, "Distance- and angle-based hybrid localization integrated in the IEEE 802.15.4 TSCH communication protocol," *Sensors*, vol. 24, no. 12, p. 3925, Jun. 2024.

GREGA MORANO (Graduate Student Member, IEEE) received the M.Sc. degree in electrical engineering from the University Of Ljubljana, in 2021. He is currently pursuing the Ph.D. degree in information and communication technologies with the Jožef Stefan International Postgraduate School.

He is currently a Research Assistant with the Department of Communication Systems, Jožef Stefan Institute, Ljubljana. His research interests include the IoT communication protocols, wireless localization, integrated sensing and communications, embedded systems, wireless sensor networks, and wireless experimental testbeds.

TOMAŽ JAVORNIK (Member, IEEE) received the B.Sc., M.Sc., and Ph.D. degrees in electrical engineering from the University of Ljubljana, Ljubljana, Slovenia, in 1987, 1990, and 1993, respectively.

He is currently a Scientific Counsellor with the Communication Systems Department, Jožef Stefan Institute, Ljubljana, and an Assistant Professor with the Jožef Stefan International Postgraduate School, Ljubljana. He participated in several COST and Framework Program projects. He has co-authored more than 100 refereed journal and conference papers and several books and book chapters in the field of mobile and wireless communications. He holds two international patents. His research experience is in the field of telecommunications, focusing on the development and performance analysis of fixed and mobile systems, radio-channel measurements, modeling and simulations, and in indoor localization. He serves as a TPC member or a reviewer for several IEEE conferences and journals.

ALEŠ SIMONČIČ (Student Member, IEEE) received the B.Sc. and M.Sc. degrees in electrical engineering from the University of Ljubljana, in 2019 and 2022, respectively. He is currently pursuing the Ph.D. degree in information and communication technologies with the Jožef Stefan International Postgraduate School.

His master's thesis focused on the estimation of the angle of arrival using BLE technology and antenna arrays. He is also a Young Researcher with the Department of Communication Systems, Jožef Stefan Institute, Ljubljana. His research interests include radio communication systems, particularly protocols, antennas and arrays, direction of arrival estimation methods, embedded systems, and radio environment characterization.

ALEŠ ŠVIGELJ (Senior Member, IEEE) received the B.Sc., M.Sc., and Ph.D. degrees in electrical engineering from the University of Ljubljana, Ljubljana, Slovenia, in 1997, 2000, and 2003 respectively.

He is currently a Senior Research Fellow with the Department of Communication Systems, Jožef Stefan Institute, and a Full Professor with the Jožef Stefan Postgraduate School. He has extensive research in modelling, simulation, and design of advanced telecommunications elements, systems, and services. He has also participated as a coordinator in several national and international projects, including COST projects. He co-authored several books/book chapters and more than 100 peer-reviewed journal and conference papers. His current work focuses on advanced networking technologies for wireless systems.

ANDREJ HROVAT (Member, IEEE) received the B.Sc. and M.Sc. degrees in electrical engineering from the University of Ljubljana, in 2004 and 2008, respectively, and the Ph.D. degree from the Jožef Stefan International Postgraduate School, in 2011.

He has been with the Department of Communication Systems, Jožef Stefan Institute, since 2004. He is currently holding the position of a senior research fellow. He works on several projects connected with professional mobile communication systems, 2G-5G, WiFi, and the IoT technologies, satellite, and sensor networks, including several COST actions, framework program projects, H2020 projects, European space agency (ESA) projects, and numerous national research and application projects. He is the author or co-author of more than 120 peer-reviewed journal and conference papers. His research and working experience are in telecommunications, focusing on development and performance analysis for fixed and mobile systems, including terrestrial, stratospheric, satellite systems, and radio-channel modeling for fixed and mobile narrowband and broadband radio communication systems. He is a TCP member of various international conferences and workshops. He is a reviewer of several international impact-factor journals. He serves on a journal editorial board member and the guest editor.

• • •